ACS APPLIED MATERIALS & INTERFACES

www.acsami.org

Research Article

Batch Fabrication of Flexible Strain Sensors with High Linearity and Low Hysteresis for Health Monitoring and Motion Detection

Boyang Liu, Binxu Lan, Liangjing Shi, Yin Cheng, Jing Sun, and Ranran Wang*

Cite This: ACS Appl. Mater. Interfaces 2024, 16, 36821−36831

Read Online

ACCESS | Metrics & More | Article Recommendations | Supporting Information

ABSTRACT: In recent years, flexible strain sensors have gradually come into our lives due to their superiority in the field of biomonitoring. However, these sensors still suffer from poor durability, high hysteresis, and difficulty in calibration, resulting in great hindrance of practical application. Herein, starting with interfacial interaction regulation and structure-induced cracking, flexible strain sensors with high performance are successfully fabricated. In this strategy, dopamine treatment is used to enhance the bonding between flexible substrates and carbon nanotubes (CNT). The combination within the conductive networks is then controlled by substituting the CNT type. Braid-like fibers are employed to achieve controllable expansion of the conductive layer cracks. Finally, we obtain strain sensors that possess high linearity (R^2 = 0.997) with low hysteresis (5%), high sensitivity (GF = 60) and wide sensing range (0−50%), short response time (62 ms), outstanding stability, and repeatability (>10,000 cycles). Flexible strain sensors with all performances good are rarely reported. Static and dynamic respiration and pulse signal monitoring by the fiber sensor are demonstrated. Moreover, a knee joint monitoring system is constructed for the monitoring of various walking stances, which is of great value to the diagnosis and rehabilitation of many diseases.

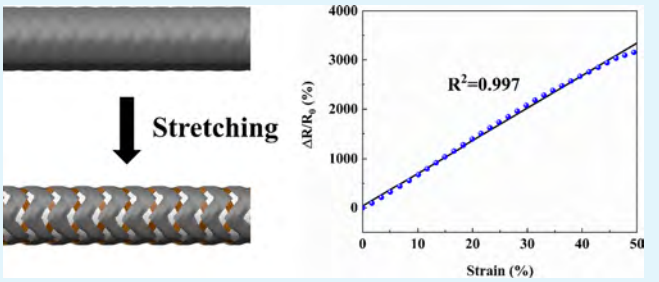

KEYWORDS: *strain sensor, wearable electronics, carbon nanotube, stretchable, fiber*

1. INTRODUCTION

In recent years, wearable electronics[1−5] have attracted widespread interest because of their immense potential in health[6−9] and robots[10−13] related fields. Among them, strain sensors form an important part with the ability to convert deformation into electrical signals, and therefore could be applied in physiological signal monitoring and motion capturing.[14−16] For strain sensors, sensitivity, and sensing range are key parameters for performance evaluation. However, conventional strain sensors fabricated by metal or semiconductor materials generally exhibit inadequate sensitivity and limited sensing range, rendering them unsuitable for wearable usage.

To solve this problem, researchers have developed strain sensors based on elastic polymers such as polydimethylsiloxane (PDMS),[17−19] thermoplastic polyurethane (TPU),[20−23] and styrene-*b*-(ethylene-*co*-butylene)-*b*-styrene (SEBS),[24−26] making successful improvement to stretchability and conformability. However, strain sensors prepared by simply combining conductive materials with flexible substrates generally fail to achieve both high sensitivity and a wide sensing range. Starting from the design of the conductive path, incorporating microstructures[27−29] such as wrinkles[30,31] and microcracks[32−34] into the sensor can ingeniously achieve synergistic enhancements between the two. Chao et al.[35] achieved the formation of a tile-like stacked hierarchical microstructure of conductive materials by a layer-by-layer spreading coating of MXene and polyaniline fiber (PANIF) on an elastic rubber substrate. The assembled strain sensor exhibited a broad sensing range (0−80%) and high sensitivity (GF = 97.6−2369.1), owing to the microcracks and spacing propagation and the reversible slippage of the overlapped MXene/PANIF sheets. Zhao et al.[36] proposed a two-step prestretching strategy and constructed a conductive layer of multiwalled carbon nanotubes (MWCNTs) with the synergistic microstructure of wrinkles and cracks on the surface of a TPU fiber with hollow-porous structure. Benefiting from the double microstructure of the conductive layer, the sensor possesses an ultrawide sensing range (0−530%) and high sensitivity (GF up to 57.2). Guo et al.[37] designed a multilevel structured fiber. It contains a porous sensing core with MXene-coated microspheres distributed in the elastic matrix (level I) and a microstructured MXene sheath with cracks (level II) embedded in wrinkle (level III)

Received: April 29, 2024
Revised: June 12, 2024
Accepted: June 19, 2024
Published: July 2, 2024

patterns. These multiple sensing levels can synergistically separately respond to various strain ranges. At small deformations, the conductive MXene@spheres embedded in the elastomer could separate from each other, providing a sensitive resistance change with small strains. At large deformations, the edges of the cracks in the MXene sheath could depart from each other, leading to a resistance increase. In addition, the wrinkles could prestore strains, thus maintaining the structural integrity of the MXene sheath at large deformations and rendering high sensitivity (GF = 174−298,000) across a wide sensing range (0−150%).

These strategies can effectively enhance both the sensing range and the sensitivity of strain sensors. However, due to the complex microstructure construction and generally poor recovery, the fabrication cost of the sensors is often high. The instability of the interfacial bonding and uncontrollable generation and expansion of cracks in the conductive layer make the sensors exhibit significant hysteresis, poor repeatability, and consistency which has significant implications for practical applications. To solve this problem, Yang et al.[38] present a computational sensor design featuring a programmed crack array within microcrumples strategy. The controllable programmed crack arrays enable the sensors to achieve exceptional repeatability (100,000 cycles) and consistency. In addition, interface optimization is also a necessary way to synergistically enhance the performance of strain sensors. Modifying the interfacial interactions through physical methods such as mechanical interlock[39] and stamping method,[40] as well as chemical methods like inducing functional groups on the surface of the substrates by UV/O_3 treatment or plasma and forming chemical bonds between the substrates and sensitive materials.[41,42] Chemical modification by functional molecules is also widely used to enhance interfacial interactions.[43,44] Yang et al.[45] enhanced the interfacial combination by embedding graphene into PDMS through the transfer of $Ti_3C_2T_X$/graphene film onto prepolymerized PDMS, resulting in a conductive material-flexible substrate interlocking structure. The brittle upper layer, mainly composed of tightly stacked irregular $Ti_3C_2T_X$ particles, then generates cracks and expands to dissipate tensile stresses. The interlocking stable interface enables this sensor to achieve excellent repeatability (over 10,000 cycles at 40% strain). The brittle upper layer causes a sharp increase in sensor resistance, resulting in high sensitivity (GF = 190.8−1148.2) when being stretched. Ren et al.[46] proposed versatile sulfur-containing CNTs by introducing abundant graphene nanoflaps on the backbone using a two-step sulfidation strategy with polysulfide and benzyl disulfide. The sulfur functionality grants a strong interfacial interaction with the elastomer polymer, while the tight graphene nanoflaps form a mechanical interlock interface with the elastomeric matrix, resulting in an enhanced combination and efficient dissipation of deformation energy. These enable the sensor to achieve excellent repeatability (≈ 30,000 cycles) and a wide working range (450%). Shi et al.[47] utilized the lubricity offered by 0D fullerenes to reduce the interlayer interaction of conductive materials. The sensor finally gained a wide sensing range (>50%), high sensitivity (GF = 25−2392.2), and low hysteresis due to the simultaneous working of propagation and slippage mechanism when stretching.

In this work, we combined interface optimization with structure-induced cracking and developed a simple method that enables scalable fabrication of strain sensors. We improved the interfacial interactions between carboxylated CNTs and braid-like polyethylene terephthalate (PET)/ polyurethane (PU) fibers through dopamine treatment and reinforced the interactions within the CNTs by adopting carboxylated CNTs and hydroxylated CNTs alternatively. The strong interfacial bonding hindered the uncontrollable sliding of CNTs which is one of the key reasons for poor repeatability, large hysteresis, and slow response. Braid-like structure of the fibers enables stress to be concentrated between PET yarns, thereby enhancing the controllability of crack formation in CNT films and facilitating the achievement of linear response and high consistency of the sensors. The obtained strain sensors finally exhibited both high sensitivity (GF = 60) and a wide working range (50%). Notably, the sensor achieved high linearity (R^2 = 0.997) and low hysteresis (5%), which are of great importance to the quantitative detection of strain. Negligible degradation was observed after cycling at 30% strain 10,000 times, and the response curve maintained constant at variable stretching speed from 0.2 to 1 mm/s, which confirmed the outstanding stability and repeatability of the sensor. The batch fabrication of the fibers has been realized. To the best of our knowledge, strain sensors with such high comprehensive performance and ease of batch production are seldom reported. The high performance of this sensor allows for the detection of joint movement and physiological signals. Based on this, we developed a smart kneepad sensing system that could assist gait analysis and facilitate accurate assessment of patients' conditions and rehabilitation progress.

2. EXPERIMENTAL SECTION

2.1. Fabrication of the Strain Sensor. Dopamine solution was prepared by diluting 1 M Tris−HCl pH 8.5 buffer solution (from Beyotime Biotechnology Co., Ltd.) with deionized water at a ratio of 1:3, and then adding dopamine hydrochloride (from Adamas Pharmaceuticals, Inc.) at a mass concentration of 2 mg/mL. The PET/PU fibers (purchased from Ruian Tizhong Ribbon Factory) were impregnated into the solution for 12 h and then washed with deionized water, followed by drying at 60 °C for 24 h to obtain dopamine-treated PET/PU fibers.

The strain-sensitive fibers were fabricated by dip coating CNTs aqueous dispersion (0.15 wt % for single-walled carbon nanotubes (SWCNTs) and 2 wt % for MWCNTs from Jiacai Technology Co., Ltd.) onto the fiber and then drying at 180 °C for 5 min.

Two conductive wires were connected to both ends of the sensor using silver pastes. After self-made silicon rubber was coated on the surface of the fiber, the strain sensor was finally obtained.

2.2. Characterizations and Tests. The SEM characterization was accomplished by a Hitachi SU8200 FE-SEM. The resistance of the sensor was measured by a True Box RC01 (from LinkZill Technology Co., Ltd.). The strain loading was implemented with a high-precision motorized linear stage (displacement resolution of 2.5 μm). The Fourier transform infrared analysis (FT-IR) spectra were obtained using a Bruker EQUINOX55.

To perform the strain response test, both ends of the fiber were secured to a glass slide. After the screws were tightened to secure the glass slide, the leads of the fibers were connected to the True Box to enable real-time monitoring of the resistance changes of the fibers during stretching.

For application demonstrations, medical tape was used to secure the sensors to the body. To measure respiration, pulse, finger flexion, wrist flexion, and elbow flexion, the sensor was attached to the abdomen and the lower chest, the front of the wrist, the interphalangeal joints, the back of the wrist joints, and the back of the elbow, respectively.

To prepare a smart kneepad sensing system, fibers were sewn onto commercial cashmere kneepads using a needle and thread. The fiber

https://doi.org/10.1021/acsami.4c07016
ACS Appl. Mater. Interfaces 2024, 16, 36821−36831

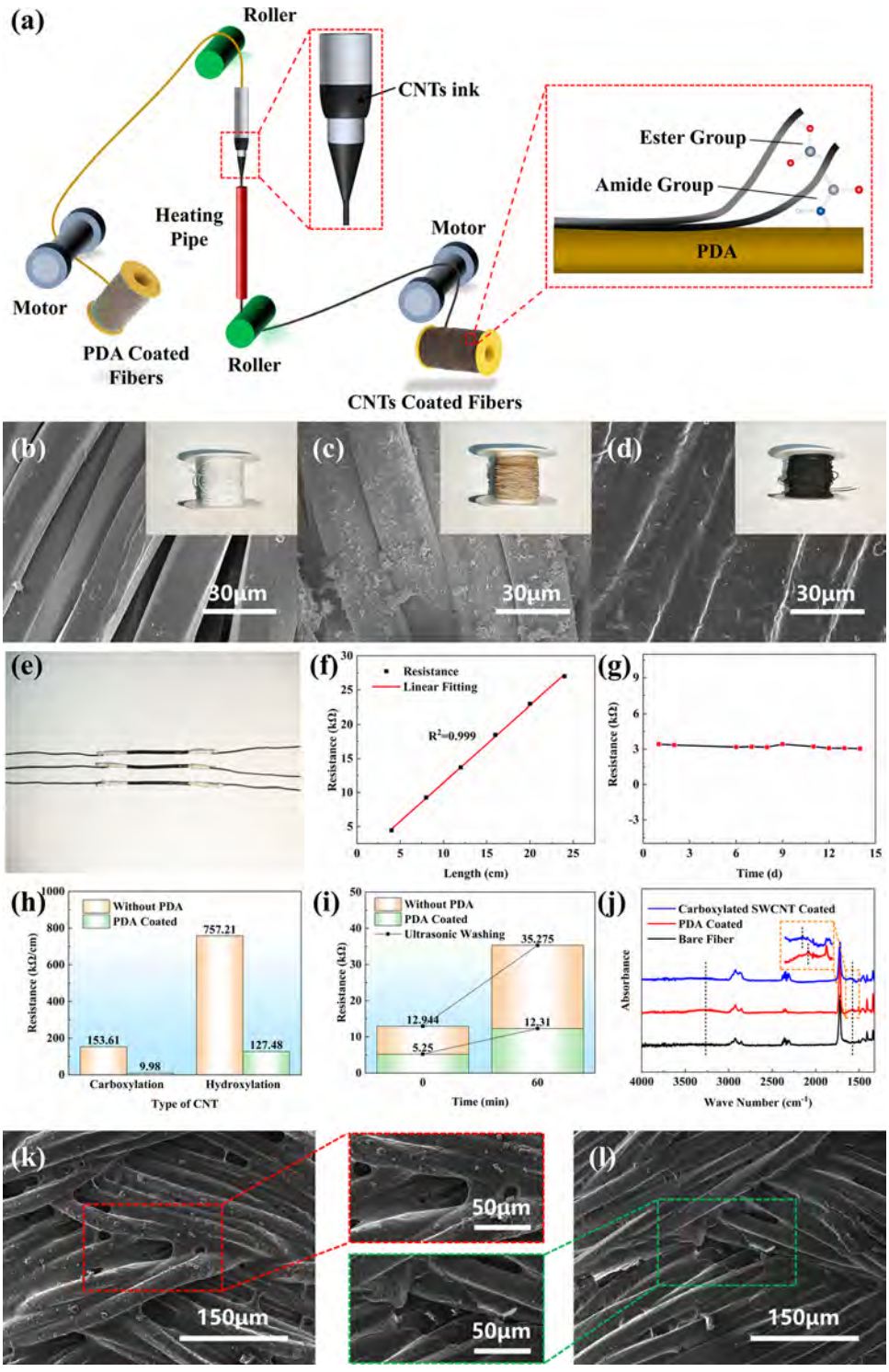

Figure 1. (a) Schematic of the working process of the continuous coating apparatus. The SEM images and photos of (b) bare fiber. (c) PDA coated fiber. (d) PDA/CNTs coated fiber. (e) Photo of sensors. (f) Resistance variation with different fiber lengths. (g) Resistance variation of the sensor during 14 days. (h) Resistance comparison of the fiber with or without the PDA layer. (i) Resistance variation with or without the PDA layer after 1 h of ultrasonic washing. (j) FT-IR spectra of bare fiber, PDA-coated fiber, and PDA/CNT-coated fiber. (k) SEM image of sensor with a PDA layer. (l) SEM image of sensor without the PDA layer.

resistance was sent to a computer in real-time via a resistance acquisition chip via Bluetooth.

3. RESULTS AND DISCUSSION

3.1. Fabrication and Characterization of Strain Sensors. We fabricated the strain-sensitive fibers using a facile method and established a continuous apparatus for the coating of CNTs and silicone rubber, as shown in Figure 1a to realize the batch production of the fibers. The dopamine-treated fibers are driven by a motor at a speed of 5 mm/s, passing through a specially designed CNT ink or liquid silicone rubber feed chute and then entering a high-temperature heated

https://doi.org/10.1021/acsami.4c07016
ACS Appl. Mater. Interfaces 2024, 16, 36821−36831

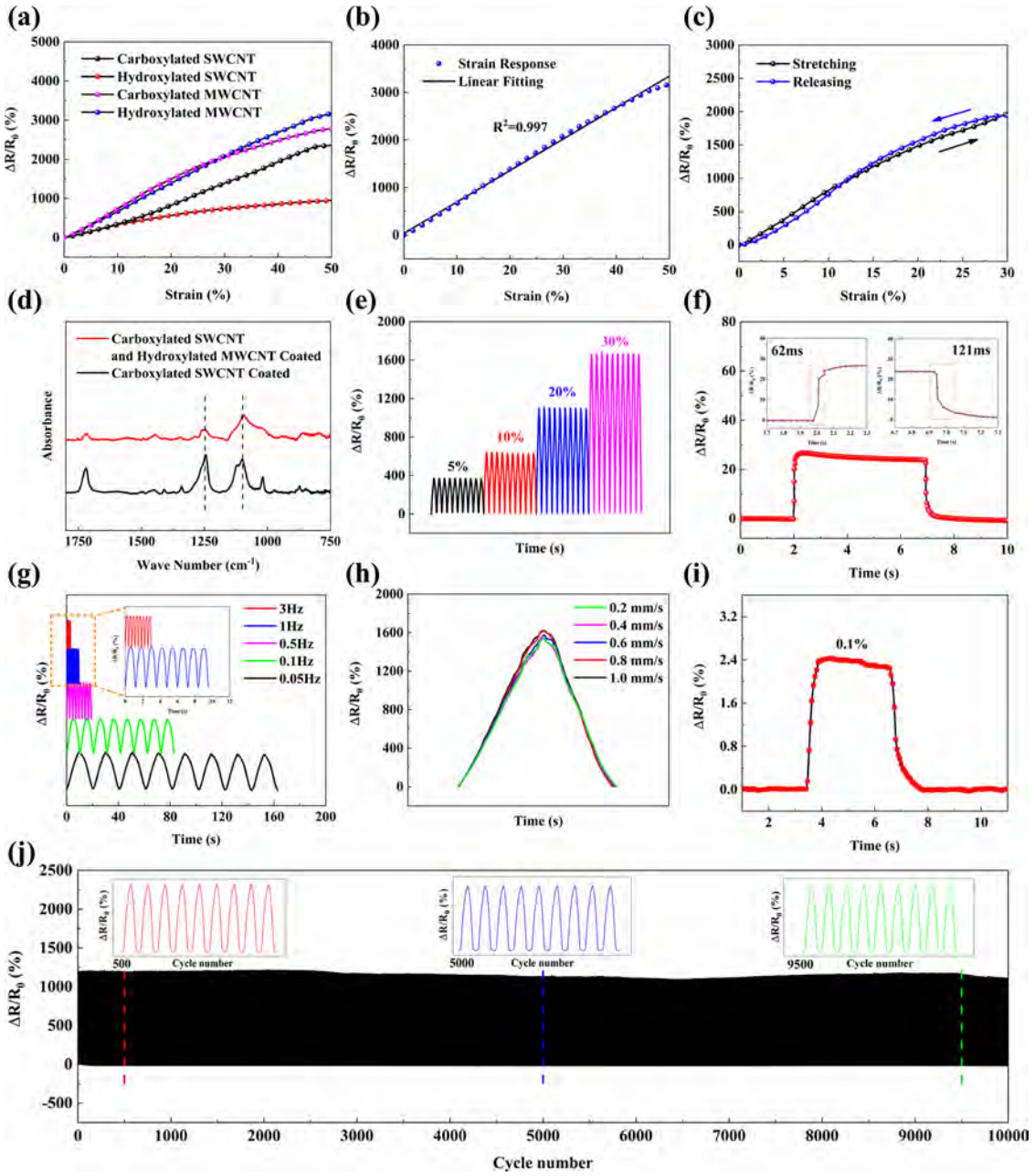

Figure 2. (a) Relative resistance variation of sensors with different types of CNTs when being stretched (strain rate of 10% per minute) up to 50% strain. (b) Relative resistance variation of sensors with carboxylated SWCNTs and hydroxylated MWCNTs. (c) Resistance variation of the strain sensor under a 30% strain stretching−releasing cycle by the rate of 0.2 mm/s. (d) FT-IR spectra of sensors with carboxylated SWCNTs and both carboxylated SWCNTs and hydroxylated MWCNTs. (e) Resistance variation of sensors under cyclic stretching at 5, 10, 20, and 30% strain. (f) Response of the sensor under 0.5% strain. (g) Resistance variation under 5% strain at the frequency of 0.05, 0.1, 0.5, 1, and 3 Hz for 8 cycles of the stretching−releasing test. (h) Resistance variation of the sensors for a single 30% stretching−releasing cycle under the rates of 0.2, 0.4, 0.6, 0.8, and 1.0 mm/s. (i) Response of the sensor under 0.1% strain. (j) Relative resistance change versus applied strain (up to 30%) over 10,000 cycles.

tube for drying at 180 °C, ultimately becoming sensing fibers with strong interfacial bonding. The substrate fiber is one kind of covered yarns with an elastic PU core fiber and polyethylene terephthalate (PET) yarns wrapping onto the core fiber with a braided arrangement. The surface and cross-section morphology of the fibers are shown in Figures 1b and S1. The overall diameter of the fiber is approximately 1 mm, with the PU core diameter of around 0.6 mm. The PET yarns are braided on the surface of the PU in bundles of 16−20 strands, with each PET strand having a diameter of about 20 μm. The elastic PU core enhances the stretchability of the fibers, while the densely woven yarn strengthens its moisture absorption, facilitating the continuous coating of the materials. Furthermore, in the braided structure, stress can be concentrated between each bundle and each strand of PET yarns, resulting in a more controllable location for crack generation in the CNT film, which facilitates the linear response of our sensors.

Without dopamine treatment, the PET/PU fibers appeared white and exhibited a smooth surface under SEM. After introducing a PDA layer through dopamine treatment, the surface morphology of the fibers changed, as shown in Figure 1c. The fibers acquired an overall yellowish-brown hue and

https://doi.org/10.1021/acsami.4c07016
ACS Appl. Mater. Interfaces 2024, 16, 36821−36831

could be observed the presence of fine particles covering their surface. These particles are the result of dopamine's self-polymerization on the fiber's surface, rendering it rougher. Subsequently, by further coating the PDA layer with carbon nanotubes (CNTs) as the sensing material, the fiber's morphology transformed, as shown in Figure 1d. Black CNTs formed a thin, dense film that conformally adhered to the fibers. Upon connecting the wires using silver adhesive and enveloping the fiber with self-made silicon rubber, we successfully fabricated the strain sensor as shown in Figure 1e. Notably, the fiber resistance increases linearly with distance, as shown in Figure 1f, exhibiting purely resistive properties. Random positions on the fiber were selected for resistance measurements, as shown in Table S1. The small fluctuations indicate that our apparatus enables a uniform coating of CNTs on the fiber surface. The resistance remains largely stable within a period of 14 days, exhibiting excellent long-term stability (Figure 1g).

Dopamine treatment effectively enhanced the combination between the CNTs and the fiber. As shown in Figure 1h, regardless of whether carboxylated or hydroxylated CNTs were coated, the introduction of PDA resulted in a significant decrease in resistance, indicating that the PDA layer could adhere to a greater number of CNTs, thereby increasing the CNT loading and reducing resistance. In addition, Figure 1i shows that strain sensors with a PDA layer (without silicon rubber on the surface) experienced a lower increase in resistance after 1 h of ultrasonic washing (134.5%). This indicates that the enhanced combination contributed by the PDA layer makes it more difficult for CNTs to detach from the fiber.

Ultimately, carboxylated CNTs achieved the lowest resistance (approximately 9.98 kΩ/cm) when combined with the PDA layer, suggesting a favorable combination with the dopamine-treated fiber. Moreover, according to strain response tests, the sensor exhibited the highest sensitivity when utilizing carboxylated single-walled CNTs (Figure S2). Consequently, for subsequent experiments, carboxylated single-walled CNTs were chosen as the first layer of conductive material.

The combination effect with or without a PDA layer between CNTs and the fiber is shown in Figure 1k, l. There exists a significant gap between the CNT layer and the substrate when the PDA is not coated. In contrast, when PDA was present on the PET surface, there was virtually no gap, indicating tight adhesion between the two parts. The tight adhesion explained the lower resistance of the fiber after coating and after the ultrasonic washing mentioned above.

To investigate the nature of the enhanced combination, we conducted FT-IR spectroscopy absorption experiments on three types of fibers: those without any treatment, those PDA coated, and those coated with CNTs (Figure 1j). The results revealed that after dopamine treatment, a wide peak corresponding to the N−H stretching vibration appeared at 3260 cm^{-1}, while a peak corresponding to the C−N stretching vibration appeared at 1577 cm^{-1}, indicating the introduction of amino groups on the fiber surface due to PDA. Upon coating with carboxylated CNT, the C−N stretching vibration peak shifted to 1581 cm^{-1}, while the peak intensity at 3260 cm^{-1} decreased. These suggest the formation of amide bonds through a reaction between the carboxyl groups and the amino groups. Therefore, PDA and carboxylated CNTs can strengthen the bonding through the formation of covalent bonds.

3.2. Performance Analysis of Strain Sensors. A strong bonding force can reduce the sliding between the CNT layer and the fiber during the stretching process, which is beneficial for improving the performance of strain sensors. However, when only a single layer of CNTs was coated, the resistance response to strain still exhibited a "J" curve with low linearity. This is because when only one layer of CNT is coated, some parts of the conductive network are more prone to breakage due to its thinness, leading to a rapid increase in resistance. Therefore, we proceeded to apply a second layer of CNTs on the sensor surface in order to achieve a more uniform conductive network and prevent the occurrence of the aforementioned problem.

Figure 2a illustrates the strain response curves of sensors after coating the second layer of various types of CNTs based on the first layer of carboxylated SWCNT. It reveals that when the second layer of hydroxylated MWCNTs was coated, the sensor exhibited the highest sensitivity (GF = 60) and linearity (R^2 = 0.997, Figure 2b). Its stress response is shown in Figure S3, with bending, torsion, and pressure response shown in Figures S4−S6. Figure 2d shows the FT-IR spectroscopy results. It demonstrates a slight shift and broadening in the absorption bands at 1100 and 1245 cm^{-1}, corresponding to the stretching vibrations of C−O−C bonds. This indicates that the esterification reaction occurred between the hydroxyl groups on the surface of the second layer of CNTs and the carboxyl groups on the surface of the first layer, enhancing the interfacial bonding inside the CNTs. This hinders the internal CNT conductive networks from responding to strain through the slipping mechanism. The introduction of PDA further prevents slip between the CNT film and the substrate, thus leading to stress dissipation primarily through crack generation. In the braided structure, crack generation is controlled between the yarns, and the distance between them uniformly increases by stretching. As a result, the increase in the sensor resistance becomes more uniform, leading to improved linearity. Furthermore, minimum slip ensures that the CNTs to be anchored at the same position on the fiber surface during both stretching and releasing processes, thus resulting in an extremely low hysteresis of approximately 5% (Figure 2c). The sensitivity of both SWCNT coatings to be applied is relatively low, with slightly higher sensitivity observed for carboxylated SWCNT. This might be attributed to the lower density of surface functional groups on SWCNT and the ability of carboxylated SWCNT to react further with residual amino groups on PDA. For comparison, Figure S7 presents the response curves of the sensor without dopamine treatment during a single stretching and recovery cycle. The sensor exhibits significant hysteresis (approximately 17%) and very low sensitivity (GF < 4) due to the severe slippage.

The strong bonding force also ensures the excellent response consistency of the sensors. Figure 2e illustrates the curves of resistance change of the sensors during 10 consecutive stretching−releasing cycles under strains of 5, 10, 20, and 30%. Each peak almost replicates the previous one under the same strain, affirming the stability of our sensors' sensing performance. Figure 2j gives the curve of resistance change of the sensors when subjected to 10,000 stretching−recovery cycles under 30% strain, revealing the persistent consistency of the sensors' response and their exceptional fatigue resistance. This outstanding consistency and fatigue resistance derive from the robust interfacial bond between the CNTs and the substrate. A strong bonding force ensures that the CNTs

https://doi.org/10.1021/acsami.4c07016
ACS Appl. Mater. Interfaces 2024, 16, 36821−36831

maintain a similar or even identical position within each cycle, enabling a highly reproducible conductive network. As a result, the resistance remains consistent after each cycle and is resistant to permanent damage.

To evaluate the response time, a 0.5% step strain was applied to the sensor rapidly. As shown in Figure 2f, the sensor demonstrated a stretching response time of 62 ms and a longer recovery response time than stretching of 121 ms because the reconstruction of the conductive pathway is slightly slower than the disconnection. This showcases its ability to respond promptly to strain. Furthermore, the sensor was subjected to frequencies of 0.05 0.1, 0.5, 1, and 3 Hz at a strain of 5%. The response signals of the sensor, as shown in Figure 2g, demonstrate its capability to discern strains up to a frequency of 3 Hz, forming distinct response curves. At low frequencies, the sensors exhibit nearly identical response curves for a single 30% stretching−releasing cycle under different rates (Figure 2h), which is important for quantitative measurement. Moreover, the sensor exhibits a minimum detectable limit of 0.1%, as depicted in Figure 2i, highlighting its ability to resolve small strains.

The mechanism by which sensors respond to strain is illustrated in Figure 3a, where the fracture of the CNT film

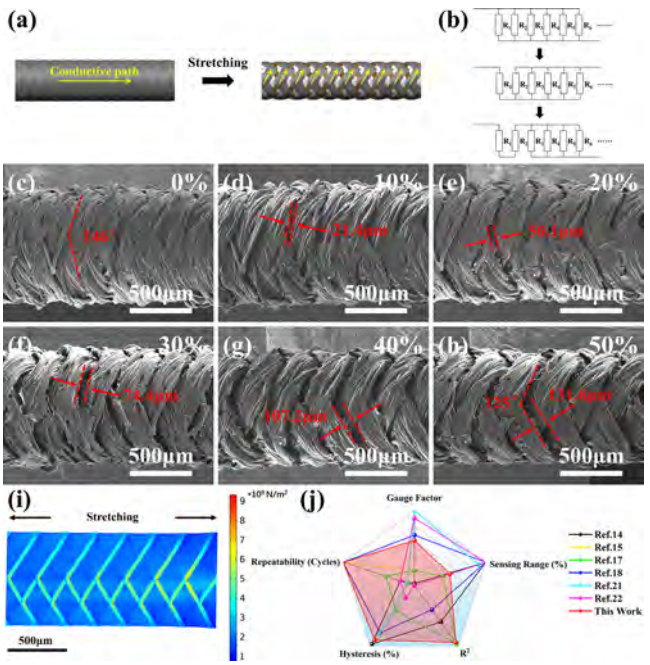

Figure 3. (a) Illustration of the fiber before and after stretching. (b) Change of the equivalent circuit diagram of the sensor during stretching. (c−h) SEM images of the sensors under various strain: 0, 10, 20, 30, 40, and 50%. (i) Finite element simulation analysis of stress distribution during stretching. (j) Comparison of GF, sensing range, linearity, hysteresis, and repeatability with recent published results.

leads to an increase in the sensor resistance. The change in the equivalent circuit diagram of the sensor is shown in Figure 3b. During the stretching process, the initially parallel arrangement of resistors gradually disconnected from each other and the spacing increases, transitioning into a series distribution, resulting in the continuous increase in resistance. SEM images of the sensor subjected to different strains are presented in Figure 3c−h with its corresponding CNTs arrangement in Figure S8. These images reveal that the PET yarns were braided together in multiple strands, forming a braidlike structure, while the CNTs are uniformly coated on the surface of the yarns. As the strain increased, because of the robust combination between the CNT film and the PET yarns, slippage was minimized, and the stress was mainly concentrated on the CNT film between the PET bundles as shown in the simulation result in Figure 3i, which resulted in the cracks to generate in the CNT film along the direction of the braided PET bundles. The cracks become wider to about 131.6 μm linearly, reducing the conductive paths. Furthermore, no visible crack generation was observed within the bundles in 0−50% strain. As a consequence, the resistance of the sensor linearly increases. Meanwhile, the braided yarns gradually tighten inward, and the angle between the two bundles shown decreased from 146° to 125°, which prevents the conductive path from being completely disconnected and ensures the response of the sensor.

In summary, compared to the recently published result (Figure 3j, in which a lower hysteresis makes a more outward point), our strain sensors exhibit rapid response, showcasing a wide frequency, high sensitivity, and strain sensing range that is substantial enough to encompass a majority of human movements. Moreover, the sensors display exceptional linearity, outstanding repeatability, and minimal hysteresis, thereby revealing great potential for application in the field of body movements and health monitoring.

3.3. Application Demonstration. Due to the high comprehensive performance, our sensors show superiority in detecting various human movements and physiological signals through strain sensing. As shown in Figure S9, it exhibits excellent washability, with the resistance change maintained within 10% during a 1 h ultrasonic washing process, which can avoid frequent replacement during usage.

When attached to the lower chest and abdomen (as shown in Figure 4a), the sensor enables respiratory monitoring of thoracic and abdominal breathing patterns. When breathing, the sensor's resistance increases due to stretching during inhalation and decreases due to recovery during exhalation. To ascertain the efficacy of sensors in detecting respiration under motion interference, we conducted ambulatory respiratory monitoring by walking simultaneously. The changes in response curves for the two breathing patterns are shown in Figure 4b, c, respectively. When monitoring thoracic breathing, the sensor exhibited only tiny fluctuations in its signal, and the waveform remained consistent, indicating a reduced level of interference when the sensor was attached to the lower chest. When monitoring abdominal respiration, larger fluctuations are observed in the signal, indicating substantial interference when the sensor is attached to the abdomen. However, effective respiratory monitoring can still be achieved by applying fast Fourier transform (FFT) filtering to remove signals above 0.5 Hz. The breathing patterns are closely related to human health, and some exercise training like yoga requires trainers to enhance abdominal breathing. In this case, our sensors are easily installed and adapt to both dynamic and static scenarios, enabling effective guidance through monitoring the relative changes in the intensity of chest and abdominal breathing signals. Little work has been reported in this domain.

When the sensor is attached to the wrist, it can perceive tiny vibrations caused by the pulse and the three characteristic peaks of percussion (P), tidal (T), and diastolic (D) can be recognized (Figure 4d). Even during the three stages of

https://doi.org/10.1021/acsami.4c07016
ACS Appl. Mater. Interfaces 2024, 16, 36821−36831

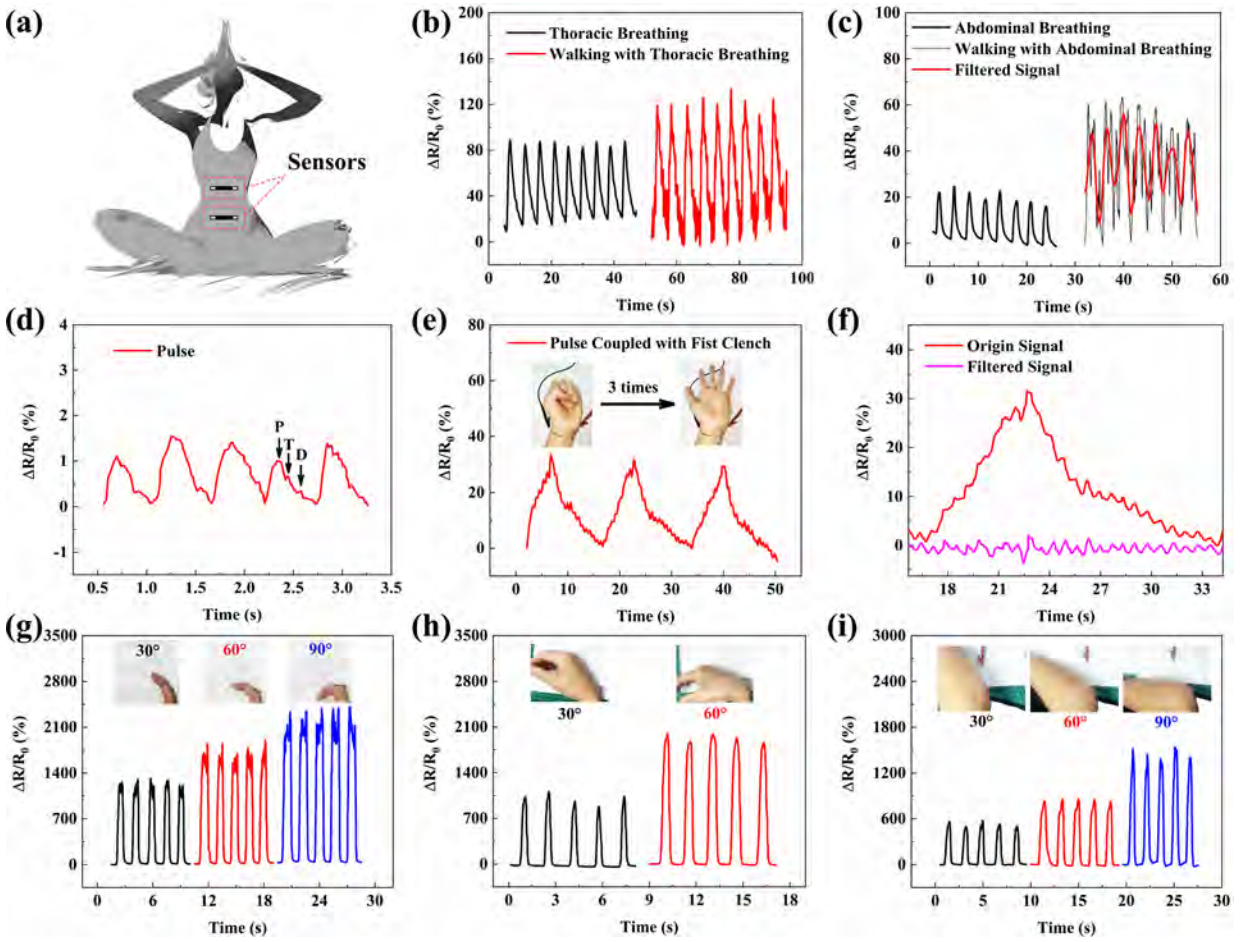

Figure 4. (a) Schematic of the sensors' attaching position. (b) Detection of thoracic breathing. (c) Detection of human breath when walking. (c) Filtered signal below 0.5 Hz for the superimposed signal by FFT filtering. (d) Detection of the pulse signal. (e) Detection of the pulse signal under 3 cycles of clenching and relaxing the fist. (f) Filtered signal above 0.5 Hz for the superimposed signal by FFT filtering. (g) Detection of finger motion. (h) Detection of wrist motion. (i) Detection of elbow motion.

clenching and relaxing the fist, small changes in the pulse signal can still be observed (Figure 4e) because of the sensor's ability to sense tiny strains with a low detection limit. Similarly, when FFT filtering is applied to the superimposed signal to remove frequencies below 0.5 Hz, the remaining signal closely matches the pulse frequency (Figure 4f). The immunity to interference is an important property for practical applications, determining whether the sensor can effectively perceive the target signal in complex environments. However, most emerging strain sensors suffer from weak interference immunity and therefore overlook its characterization and discussion.[48] The above experiments show that our sensors have exceptional immunity to interference due to their remarkably low hysteresis and rapid, accurate, and stable response to strain.

Furthermore, when the sensors are attached to the joints, bending the joints at different angles can cause varying degrees of resistance change. Figure 4g–i demonstrates its sensing capability when attached to the finger, wrist, and elbow joints. The signals from the sensors increase as the bending angle increases, and they remain relatively consistent throughout five repetitive cycles. This indicates the potential of strain sensors to monitor body movements by sensing joint bending.

The lower limbs of the human body are very susceptible to disease or aging, which can lead to abnormalities in their movement. Therefore, gait analysis is a frequently employed method to understand the physical condition of the body. A comprehensive gait analysis can provide valuable insights into medical rehabilitation, expediting patients' recovery, and preventing long-term injuries caused by poor posture. Traditional gait analysis usually must be performed at a specific location, which imposes significant spatial constraints. However, due to the rapid growth of the aging population and the significant challenges posed by global epidemics to public health, there exists a growing interest in developing more convenient real-time health monitoring systems. Among them, flexible wearable sensors are more comfortable to use, presenting significant potential for applications. Consequently, we verified the capability of the fabricated sensors to collect motion data and apply them to gait analysis.

We integrated the sensor, a cashmere elastic kneepad, a resistive acquisition chip with Bluetooth transmission capability, and a lithium battery into a smart kneepad sensing system (Figure 5a). Figure 5b illustrates the workflow of this system. Powered by a lithium battery, the resistive acquisition chip continuously captures real-time variations in the sensor's resistance and wirelessly transmits the data to a computer via Bluetooth. As the knee joint moves, inducing strain on the sensor, corresponding changes in the resistance curve become observable on the computer through specific software.

https://doi.org/10.1021/acsami.4c07016
ACS Appl. Mater. Interfaces 2024, 16, 36821−36831

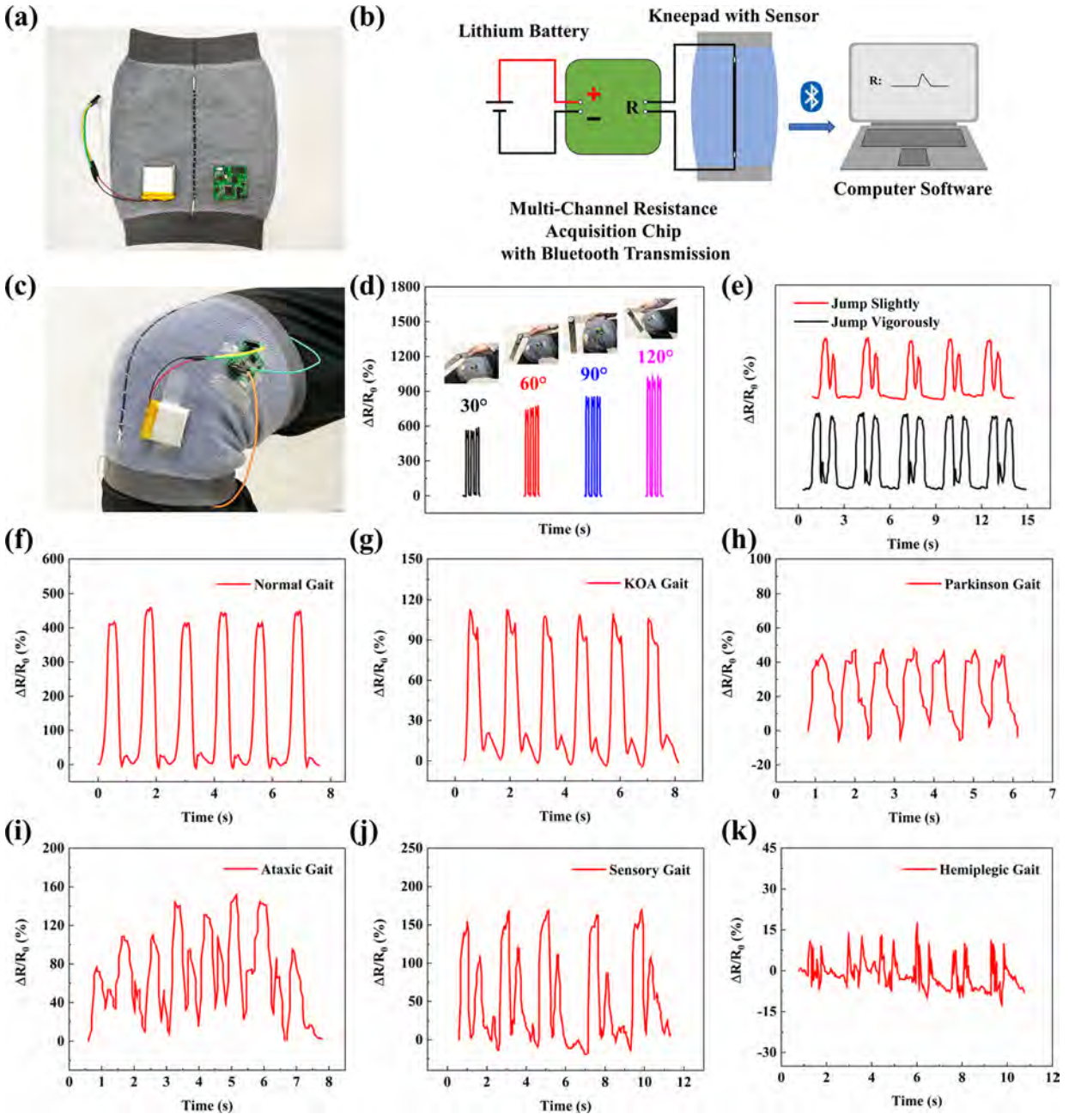

Figure 5. (a) Photo of smart kneepad sensing system. (b) Schematic of the working process of the smart kneepad sensing system. (c) Photograph of the smart kneepad sensing system when worn on the knee joint. (d) Resistance response of knee flexion. (e) Resistance response of jump. (f) Resistance response of normal gait. (g) Resistance response of KOA gait. (h) Resistance response of Parkinson gait. (i) Resistance response of ataxic gait. (j) Resistance response of sensory gait. (k) Resistance response of hemiplegic gait.

After the kneepad is worn as Figure 5c shows, Figure 5d illustrates the signal response when bending the knee joint to 30°, 60°, 90°, and 120°. The sensor's resistance increased with the increasing angle of knee flexion, indicating its ability to discern the angle of knee flexion. Based on this, it is capable of recognizing various movements related to the knee joint. Figure 5e presents the sensing curve of the smart kneepad for different intensities of jumping. During a slight jump, the sensor generates two distinct peaks corresponding to the knee joint flexion during the process of power storage before jumping and the buffer after landing. During a vigorous jump, the peak associated with the landing buffer significantly rises, indicating that the knee joint bent to a greater angle to absorb the impact upon landing. Additionally, the hang time between the two peaks noticeably lengthens. Furthermore, due to the lengthened hang time, the knee joint gradually undergoes a natural flexion, resulting in the generation of a weak peak between the two main peaks.

In addition to discerning subtle differences in regular motion, our sensors can also integrate with medical rehabilitation and diagnosis by utilizing the characteristics of different knee joint motions in a common clinical gait for gait analysis. We employed methods such as volunteer recruitment, scenario simulation, or feature imitation to test the sensing curve of the smart kneepad for different gait patterns. When a healthy volunteer walked normally (Figure 5f), the gait curve

https://doi.org/10.1021/acsami.4c07016
ACS Appl. Mater. Interfaces 2024, 16, 36821−36831

exhibited two peaks, corresponding to the two flexion movements of the knee joint during the swing and support phases. When a volunteer suffers from knee osteoarthritis (KOA) (Figure 5g), the curve does not descend to the lowest point during the transition from the swing phase to the support phase. This indicates that the patient's knee joint remained in a bent position, which can help reduce the load on the knee joint and alleviate the pain caused by KOA. Figure 5h depicts the gait curve when the tester imitates the gait of Parkinson's patients. Due to the extensive joint flexion and limited range of motion experienced by them, the variation in the knee joint flexion angle during walking is minimal, resulting in lower peak values. Furthermore, the higher stride frequency and lower swing phase proportion contribute to the presence of only a single peak in each gait cycle. Figure 5i depicts the gait curve when the tester was intoxicated, commonly known as an ataxic gait. This gait is often caused by intoxication or cerebellar lesions, characterized by unsteady and stumbling walking with impaired balance. As a result, although the peaks created by knee flexion during the swing and support phases still exist in the curve, they appear more erratic. Figure 5j illustrates the gait curve when the tester was walking in a dark environment, commonly known as the sensory gait. This gait typically indicates a dissociation between foot contact with the ground and the brain's reception of position information. At this moment, people elevate their legs and firmly plant their feet on the ground in order to perceive information on position. During this process, there is a posterior shift of the body's center of mass, leading to an increase in the flexion angle of the knee joint during both the swing and support phases, resulting in an amplified peak value of the curve. Figure 5k illustrates the gait curve of the testers when imitating the gait of hemiplegic patients. Due to the excessive extensor muscle tone in the affected lower limb, flexion is severely limited, resulting in minimal peak values during both the swing and support phases.

In summary, the smart kneepad sensing system is able to monitor gait by sensing knee joint motion and provide valuable insights for medical rehabilitation, expediting patients' recovery, and preventing long-term injuries caused by poor posture. It exhibits promising prospects for application in the realm of body movement and health monitoring.

4. CONCLUSIONS

In this paper, we have developed a simple method by strengthening the interfacial interaction inside the strain sensor for its large-scale fabrication to achieve low hysteresis (5%), outstanding repeatability (10,000 cycles), and high linearity (R^2 = 0.997). It may provide insights from the perspective of interface optimization. Additionally, we present the demonstrated applications of the fabricated sensors in various body movements and health monitoring, with a particular focus on static and dynamic respiration and exploring their potential application in gait analysis to facilitate accurate assessment of patients' conditions and rehabilitation progress. We believe this sensor holds immense potential for applications.

■ ASSOCIATED CONTENT

Supporting Information

The Supporting Information is available free of charge at https://pubs.acs.org/doi/10.1021/acsami.4c07016.

Surface and cross-section SEM images of the fiber; random resistance of the fiber; relative resistance variation of sensors with different types of CNTs coated on the first layer when being stretched; strain−stress curves for 5 cycles; resistance variation of the sensor during bending; resistance variation of the sensor in the torsion test from −81 to 81 rad/m; resistance variation of the sensor in the pressure test; SEM images of the CNTs arrangement during stretching; and resistance variation of the sensor during 1 h of ultrasonic washing (PDF)

■ AUTHOR INFORMATION

Corresponding Author

Ranran Wang − *State Key Laboratory of High Performance Ceramics and Superfine Microstructure, Shanghai Institute of Ceramics, Chinese Academy of Sciences, Shanghai 200050, China; School of Chemistry and Materials Science, Hangzhou Institute for Advanced Study, University of Chinese Academy of Sciences, Hangzhou 310024, China;* orcid.org/0000-0001-5097-2834; Email: wangranran@mail.sic.ac.cn

Authors

Boyang Liu − *State Key Laboratory of High Performance Ceramics and Superfine Microstructure, Shanghai Institute of Ceramics, Chinese Academy of Sciences, Shanghai 200050, China; School of Chemistry and Materials Science, Hangzhou Institute for Advanced Study, University of Chinese Academy of Sciences, Hangzhou 310024, China; Center of Materials Science and Optoelectronics Engineering, University of Chinese Academy of Sciences, Beijing 100049, China*

Binxu Lan − *State Key Laboratory of High Performance Ceramics and Superfine Microstructure, Shanghai Institute of Ceramics, Chinese Academy of Sciences, Shanghai 200050, China*

Liangjing Shi − *State Key Laboratory of High Performance Ceramics and Superfine Microstructure, Shanghai Institute of Ceramics, Chinese Academy of Sciences, Shanghai 200050, China*

Yin Cheng − *State Key Laboratory of High Performance Ceramics and Superfine Microstructure, Shanghai Institute of Ceramics, Chinese Academy of Sciences, Shanghai 200050, China*

Jing Sun − *State Key Laboratory of High Performance Ceramics and Superfine Microstructure, Shanghai Institute of Ceramics, Chinese Academy of Sciences, Shanghai 200050, China;* orcid.org/0000-0003-1101-1584

Complete contact information is available at: https://pubs.acs.org/10.1021/acsami.4c07016

Notes

The authors declare no competing financial interest.

■ ACKNOWLEDGMENTS

This work was financially supported by the National Natural Science Foundation of China (Grant No. 62122080, 62261136551) and the Natural Science Foundation of Shanghai (22ZR1481700, 22dz1205000).

■ REFERENCES

(1) Gao, L.; Hu, B.-L.; Wang, L.; Cao, J.; He, R.; Zhang, F.; Wang, Z.; Xue, W.; Yang, H.; Li, R.-W. Intrinsically elastic polymer ferroelectric by precise slight cross-linking. *Science* **2023**, *381* (6657), 540−544.

(2) Liu, W.; Liu, Y.; Yang, Z.; Xu, C.; Li, X.; Huang, S.; Shi, J.; Du, J.; Han, A.; Yang, Y.; Xu, G.; Yu, J.; Ling, J.; Peng, J.; Yu, L.; Ding, B.; Gao, Y.; Jiang, K.; Li, Z.; Yang, Y.; Li, Z.; Lan, S.; Fu, H.; Fan, B.; Fu, Y.; He, W.; Li, F.; Song, X.; Zhou, Y.; Shi, Q.; Wang, G.; Guo, L.; Kang, J.; Yang, X.; Li, D.; Wang, Z.; Li, J.; Thoroddsen, S.; Cai, R.; Wei, F.; Xing, G.; Xie, Y.; Liu, X.; Zhang, L.; Meng, F.; Di, Z.; Liu, Z. Flexible solar cells based on foldable silicon wafers with blunted edges. *Nature* **2023**, *617* (7962), 717−723.
(3) Cheng, X.; Zhang, F.; Bo, R.; Shen, Z.; Pang, W.; Jin, T.; Song, H.; Xue, Z.; Zhang, Y. An Anti-Fatigue Design Strategy for 3D Ribbon-Shaped Flexible Electronics. *Adv. Mater.* **2021**, *33* (37), No. 2102684.
(4) Li, L.; Zheng, Z.; Ge, C.; Wang, Y.; Dai, H.; Li, L.; Wang, S.; Gao, Q.; Liu, M.; Sun, F.; Zhang, T. A Flexible Tough Hydrovoltaic Coating for Wearable Sensing Electronics. *Adv. Mater.* **2023**, *35* (40), No. 2304099.
(5) Shi, X.; Zuo, Y.; Zhai, P.; Shen, J.; Yang, Y.; Gao, Z.; Liao, M.; Wu, J.; Wang, J.; Xu, X.; Tong, Q.; Zhang, B.; Wang, B.; Sun, X.; Zhang, L.; Pei, Q.; Jin, D.; Chen, P.; Peng, H. Large-area display textiles integrated with functional systems. *Nature* **2021**, *591* (7849), 240−245.
(6) Sun, C.; Liu, X.; Yao, Q.; Jiang, Q.; Xia, X.; Shen, Y.; Ye, X.; Tan, H.; Gao, R.; Zhu, X.; Li, R.-W. A Discolorable Flexible Synaptic Transistor for Wearable Health Monitoring. *ACS Nano* **2024**, *18* (1), 515−525.
(7) Hou, Y.; Yang, Y.; Wang, Z.; Li, Z.; Zhang, X.; Bethers, B.; Xiong, R.; Guo, H.; Yu, H. Whole Fabric-Assisted Thermoelectric Devices for Wearable Electronics. *Adv. Sci.* **2022**, *9* (1), No. 2103574.
(8) Cheng, J.; Shang, J.; Yang, S.; Dou, J.; Shi, X.; Jiang, X. Wet-Adhesive Elastomer for Liquid Metal-Based Conformal Epidermal Electronics. *Adv. Funct. Mater.* **2022**, *32* (25), No. 2200444.
(9) Cheng, Y.; Wang, R.; Chan, K. H.; Lu, X.; Sun, J.; Ho, G. W. A Biomimetic Conductive Tendril for Ultrastretchable and Integratable Electronics, Muscles, and Sensors. *ACS Nano* **2018**, *12* (4), 3898−3907.
(10) Pang, Y.; Xu, X.; Chen, S.; Fang, Y.; Shi, X.; Deng, Y.; Wang, Z.-L.; Cao, C. Skin-inspired textile-based tactile sensors enable multifunctional sensing of wearables and soft robots. *Nano Energy* **2022**, *96*, No. 107137.
(11) Wang, L.; Li, N.; Zhang, Y.; Di, P.; Li, M.; Lu, M.; Liu, K.; Li, Z.; Ren, J.; Zhang, L.; Wan, P. Flexible multiresponse-actuated nacre-like MXene nanocomposite for wearable human-machine interfacing. *MATTER* **2022**, *5* (10), 3417−3431.
(12) Ying, B.; Chen, R. Z.; Zuo, R.; Li, J.; Liu, X. An Anti-Freezing, Ambient-Stable and Highly Stretchable Ionic Skin with Strong Surface Adhesion for Wearable Sensing and Soft Robotics. *Adv. Funct. Mater.* **2021**, *31* (42), No. 2104665.
(13) Shen, T.; Liu, S.; Yue, X.; Wang, Z.; Liu, H.; Yin, R.; Liu, C.; Shen, C. High-performance fibrous strain sensor with synergistic sensing layer for human motion recognition and robot control. *Adv. Compos. Hybrid Mater.* **2023**, *6* (4), 127.
(14) Shen, Z.; Zhang, Z.; Zhang, N.; Li, J.; Zhou, P.; Hu, F.; Rong, Y.; Lu, B.; Gu, G. High-Stretchability, Ultralow-Hysteresis ConductingPolymer Hydrogel Strain Sensors for Soft Machines. *Adv. Mater.* **2022**, *34* (32), No. 2203650.
(15) Wu, S.-D.; Hsu, S.-H.; Ketelsen, B.; Bittinger, S. C.; Schlicke, H.; Weller, H.; Vossmeyer, T. Fabrication of Eco-Friendly Wearable Strain Sensor Arrays via Facile Contact Printing for Healthcare Applications. *Small Methods* **2023**, *7* (9), No. 2300170.
(16) Cheng, Y.; Lu, X.; Hoe Chan, K.; Wang, R.; Cao, Z.; Sun, J.; Wei Ho, G. A stretchable fiber nanogenerator for versatile mechanical energy harvesting and self-powered full-range personal healthcare monitoring. *Nano Energy* **2017**, *41*, 511−518.
(17) Jo, H.; Park, J.-S.; Lim, H.-Y.; Lee, G.-Y. Laser Sintered Silver Nanoparticles on the PDMS for a Wearable Strain Sensor Capable of Detecting Finger Motion. *ACS Appl. Nano Mater.* **2023**, *6* (24), 22998−23011.
(18) Hu, M.; Gao, Y.; Jiang, Y.; Zeng, H.; Zeng, S.; Zhu, M.; Xu, G.; Sun, L. High-performance strain sensors based on bilayer carbon black/PDMS hybrids. *Adv. Compos. Hybrid Mater.* **2021**, *4* (3), 514−520.
(19) Dai, Z.; Ding, S.; Lei, M.; Li, S.; Xu, Y.; Zhou, Y.; Zhou, B. A superhydrophobic and anti-corrosion strain sensor for robust underwater applications. *J. Mater. Chem. A* **2021**, *9* (27), 15282−15293.
(20) Wang, L.; Chen, Y.; Lin, L.; Wang, H.; Huang, X.; Xue, H.; Gao, J. Highly stretchable, anti-corrosive and wearable strain sensors based on the PDMS/CNTs decorated elastomer nanofiber composite. *Chem. Eng. J.* **2019**, *362*, 89−98.
(21) Shen, Y.; Yang, W.; Hu, F.; Zheng, X.; Zheng, Y.; Liu, H.; Algadi, H.; Chen, K. Ultrasensitive wearable strain sensor for promising application in cardiac rehabilitation. *Adv. Compos. Hybrid Mater.* **2022**, *6* (1), 21.
(22) Wang, H.; Zhou, R.; Li, D.; Zhang, L.; Ren, G.; Wang, L.; Liu, J.; Wang, D.; Tang, Z.; Lu, G.; Sun, G.; Yu, H.-D.; Huang, W. High-Performance Foam-Shaped Strain Sensor Based on Carbon Nanotubes and Ti3C2Tx MXene for the Monitoring of Human Activities. *ACS Nano* **2021**, *15* (6), 9690−9700.
(23) Yue, X.; Fang, C.; Yao, Q.; Liu, C.; Shen, C.; Liu, H. Tunable porous fiber-shaped strain sensor with synergistic conductive network for human motion recognition and tactile sensing. *Chem. Eng. J.* **2024**, *491*, No. 151853.
(24) Shen, Z.; Feng, J. Mass-produced SEBS/graphite nanoplatelet composites with a segregated structure for highly stretchable and recyclable strain sensors. *J. Mater. Chem. C* **2019**, *7* (30), 9423−9429.
(25) Cui, X.; Jiang, Y.; Xu, Z.; Xi, M.; Jiang, Y.; Song, P.; Zhao, Y.; Wang, H. Stretchable strain sensors with dentate groove structure for enhanced sensing recoverability. *Composites, Part B* **2021**, *211*, No. 108641.
(26) Dong, J.; Li, L.; Zhang, C.; Ma, P.; Dong, W.; Huang, Y.; Liu, T. Ultra-highly stretchable and anisotropic SEBS/F127 fiber films equipped with an adaptive deformable carbon nanotube layer for dual-mode strain sensing. *J. Mater. Chem. A* **2021**, *9* (34), 18294−18305.
(27) Gu, C.; Qin, W.; Wang, Y.; Li, X.; Wang, J.; Tian, Z.; Yang, M.; Qiao, H.; Wu, Y.; Yin, S. Highly stretchable, durable, and superfine fiber-shaped strain sensor with a porous core-sheath microstructure. *Compos. Commun.* **2022**, *36*, No. 101381.
(28) Shen, G.; Chen, B.; Liang, T.; Liu, Z.; Zhao, S.; Liu, J.; Zhang, C.; Yang, W.; Wang, Y.; He, X. Transparent and Stretchable Strain Sensors with Improved Sensitivity and Reliability Based on Ag NWs and PEDOT:PSS Patterned Microstructures. *Adv. Electron. Mater.* **2020**, *6* (8), No. 1901360.
(29) Sun, H.; Bu, Y.; Liu, H.; Wang, J.; Yang, W.; Li, Q.; Guo, Z.; Liu, C.; Shen, C. Superhydrophobic conductive rubber band with synergistic dual conductive layer for wide-range sensitive strain sensor. *Sci. Bull.* **2022**, *67* (16), 1669−1678.
(30) Chu, Z.; Jiao, W.; Huang, Y.; Zheng, Y.; Wang, R.; He, X. Superhydrophobic gradient wrinkle strain sensor with ultra-high sensitivity and broad strain range for motion monitoring. *J. Mater. Chem. A* **2021**, *9* (15), 9634−9643.
(31) Zhu, T.; Wu, K.; Xia, Y.; Yang, C.; Chen, J.; Wang, Y.; Zhang, J.; Pu, X.; Liu, G.; Sun, J. Topological Gradients for Metal Film-Based Strain Sensors. *Nano Lett.* **2022**, *22* (16), 6637−6646.
(32) Guo, X.; Hong, W.; Zhao, Y.; Zhu, T.; Liu, L.; Li, H.; Wang, Z.; Wang, D.; Mai, Z.; Zhang, T.; Yang, J.; Zhang, F.; Xia, Y.; Hong, Q.; Xu, Y.; Yan, F.; Wang, M.; Xing, G. Bioinspired Dual-Mode Stretchable Strain Sensor Based on Magnetic Nanocomposites for Strain/Magnetic Discrimination. *Small* **2023**, *19* (1), No. 2205316.
(33) Sun, H.; Dai, K.; Zhai, W.; Zhou, Y.; Li, J.; Zheng, G.; Li, B.; Liu, C.; Shen, C. A Highly Sensitive and Stretchable Yarn Strain Sensor for Human Motion Tracking Utilizing a Wrinkle-Assisted Crack Structure. *ACS Appl. Mater. Interfaces* **2019**, *11* (39), 36052−36062.
(34) Tian, Y.; Huang, M.; Wang, Y.; Zheng, Y.; Yin, R.; Liu, H.; Liu, C.; Shen, C. Ultra-stretchable, sensitive and breathable electronic skin based on TPU electrospinning fibrous membrane with microcrack

structure for human motion monitoring and self-powered application. *Chem. Eng. J.* **2024**, *480*, No. 147899.
(35) Chao, M.; Wang, Y.; Ma, D.; Wu, X.; Zhang, W.; Zhang, L.; Wan, P. Wearable MXene nanocomposites-based strain sensor with tile-like stacked hierarchical microstructure for broad-range ultra-sensitive sensing. *Nano Energy* **2020**, *78*, No. 105187.
(36) Zhao, X.; Guo, H.; Ding, P.; Zhai, W.; Liu, C.; Shen, C.; Dai, K. Hollow-porous fiber-shaped strain sensor with multiple wrinkle-crack microstructure for strain visualization and wind monitoring. *Nano Energy* **2023**, *108*, No. 108197.
(37) Guo, Q.; Pang, W.; Xie, X.; Xu, Y.; Yuan, W. Stretchable, conductive and porous MXene-based multilevel structured fibers for sensitive strain sensing and gas sensing. *J. Mater. Chem. A* **2022**, *10* (29), 15634−15646.
(38) Yang, H.; Ding, S.; Wang, J.; Sun, S.; Swaminathan, R.; Ng, S. W. L.; Pan, X.; Ho, G. W. Computational design of ultra-robust strain sensors for soft robot perception and autonomy. *Nat. Commun.* **2024**, *15* (1), 1636.
(39) Xu, Y.; Chen, L.; Chen, J.; Chang, X.; Zhu, Y. Flexible and Transparent Pressure/Temperature Sensors Based on Ionogels with Bioinspired Interlocked Microstructures. *ACS Appl. Mater. Interfaces* **2022**, *14* (1), 2122−2131.
(40) Liang, B.; Zhang, Z.; Chen, W.; Lu, D.; Yang, L.; Yang, R.; Zhu, H.; Tang, Z.; Gui, X. Direct Patterning of Carbon Nanotube via Stamp Contact Printing Process for Stretchable and Sensitive Sensing Devices. *Nano Micro Lett.* **2019**, *11* (1), 92.
(41) Sun, C.; Zhang, J.; Zhang, Y.; Zhao, F.; Xie, J.; Liu, Z.; Zhuang, J.; Zhang, N.; Ren, W.; Ye, Z.-G. Design and fabrication of flexible strain sensor based on ZnO-decorated PVDF via atomic layer deposition. *Appl. Surf. Sci.* **2021**, *562*, No. 150126.
(42) Yang, S.; Yang, W.; Yin, R.; Liu, H.; Sun, H.; Pan, C.; Liu, C.; Shen, C. Waterproof conductive fiber with microcracked synergistic conductive layer for high-performance tunable wearable strain sensor. *Chem. Eng. J.* **2023**, *453*, No. 139716.
(43) Wang, J.; Lin, J.; Pan, K.; Zhang, K.; Zhang, H.; Dong, J.; Hu, D.; Jia, Z.; Luo, J. A sparse-dense hierarchical structured conductive elastomer composites for highly sensitive and stretchable strain sensor. *Chem. Eng. J.* **2023**, *477*, No. 146759.
(44) Li, W.; Tao, L.-Q.; Kang, M.-C.; Li, C.-H.; Luo, C.-Y.; He, G.; Sang, T.-Y.; Wang, P. Tunable mechanical, self-healing hydrogels driven by sodium alginate and modified carbon nanotubes for health monitoring. *Carbohydr. Polym.* **2022**, *295*, No. 119854.
(45) Yang, Y.; Cao, Z.; He, P.; Shi, L.; Ding, G.; Wang, R.; Sun, J. Ti3C2Tx MXene-graphene composite films for wearable strain sensors featured with high sensitivity and large range of linear response. *Nano Energy* **2019**, *66*, No. 104134.
(46) Ren, D.; Zhao, C.; Zhang, S.; Zhang, K.; Huang, F. Novel Sulfur-Containing Carbon Nanotubes with Graphene Nanoflaps for Stretchable Sensing, Joule Heating, and Electro-Thermal Actuating. *Adv. Funct. Mater.* **2023**, *33* (21), No. 2300517.
(47) Shi, X.; Liu, S.; Sun, Y.; Liang, J.; Chen, Y. Lowering Internal Friction of 0D−1D−2D Ternary Nanocomposite-Based Strain Sensor by Fullerene to Boost the Sensing Performance. *Adv. Funct. Mater.* **2018**, *28* (22), No. 1800850.
(48) Bai, Z.; Wang, X.; Huang, M.; Zheng, M.; Yue, O.; Hao, D.; Wang, Y.; Zou, X.; Cui, B.; Xie, L.; Zha, S.; Ju, H.; Liu, X. Versatile nano−micro collagen fiber-based wearable electronics for health monitoring and thermal management. *J. Mater. Chem. A* **2023**, *11* (2), 726−741.

https://doi.org/10.1021/acsami.4c07016
ACS Appl. Mater. Interfaces 2024, 16, 36821−36831